NASA/TM—2020-220235

Heat Transfer Measurements and Computations on Blade of Variable Speed Power Turbine Blade Cascade

Philip E. Poinsatte
Glenn Research Center, Cleveland, Ohio

Douglas R. Thurman
U.S. Army Research Laboratory, Glenn Research Center, Cleveland, Ohio

Paul W. Giel
Vantage Partners, LLC, Brook Park, Ohio

Ali A. Ameri
The Ohio State University, Columbus, Ohio

Barbara L. Lucci
Glenn Research Center, Cleveland, Ohio

June 2020

NASA STI Program . . . in Profile

Since its founding, NASA has been dedicated to the advancement of aeronautics and space science. The NASA Scientific and Technical Information (STI) Program plays a key part in helping NASA maintain this important role.

The NASA STI Program operates under the auspices of the Agency Chief Information Officer. It collects, organizes, provides for archiving, and disseminates NASA's STI. The NASA STI Program provides access to the NASA Technical Report Server—Registered (NTRS Reg) and NASA Technical Report Server—Public (NTRS) thus providing one of the largest collections of aeronautical and space science STI in the world. Results are published in both non-NASA channels and by NASA in the NASA STI Report Series, which includes the following report types:

- TECHNICAL PUBLICATION. Reports of completed research or a major significant phase of research that present the results of NASA programs and include extensive data or theoretical analysis. Includes compilations of significant scientific and technical data and information deemed to be of continuing reference value. NASA counter-part of peer-reviewed formal professional papers, but has less stringent limitations on manuscript length and extent of graphic presentations.

- TECHNICAL MEMORANDUM. Scientific and technical findings that are preliminary or of specialized interest, e.g., "quick-release" reports, working papers, and bibliographies that contain minimal annotation. Does not contain extensive analysis.

- CONTRACTOR REPORT. Scientific and technical findings by NASA-sponsored contractors and grantees.

- CONFERENCE PUBLICATION. Collected papers from scientific and technical conferences, symposia, seminars, or other meetings sponsored or co-sponsored by NASA.

- SPECIAL PUBLICATION. Scientific, technical, or historical information from NASA programs, projects, and missions, often concerned with subjects having substantial public interest.

- TECHNICAL TRANSLATION. English-language translations of foreign scientific and technical material pertinent to NASA's mission.

For more information about the NASA STI program, see the following:

- Access the NASA STI program home page at http://www.sti.nasa.gov

- E-mail your question to help@sti.nasa.gov

- Fax your question to the NASA STI Information Desk at 757-864-6500

- Telephone the NASA STI Information Desk at 757-864-9658

- Write to:
  NASA STI Program
  Mail Stop 148
  NASA Langley Research Center
  Hampton, VA 23681-2199

NASA/TM—2020-220235

Heat Transfer Measurements and Computations on Blade of Variable Speed Power Turbine Blade Cascade

Philip E. Poinsatte
Glenn Research Center, Cleveland, Ohio

Douglas R. Thurman
U.S. Army Research Laboratory, Glenn Research Center, Cleveland, Ohio

Paul W. Giel
Vantage Partners, LLC, Brook Park, Ohio

Ali A. Ameri
The Ohio State University, Columbus, Ohio

Barbara L. Lucci
Glenn Research Center, Cleveland, Ohio

National Aeronautics and
Space Administration

Glenn Research Center
Cleveland, Ohio 44135

June 2020

Acknowledgments

This work was supported by the Revolutionary Vertical Lift Project at the NASA Glenn Research Center.

This work was sponsored by the Advanced Air Vehicle Program
at the NASA Glenn Research Center

Level of Review: This material has been technically reviewed by technical management.

Available from

NASA STI Program
Mail Stop 148
NASA Langley Research Center
Hampton, VA 23681-2199

National Technical Information Service
5285 Port Royal Road
Springfield, VA 22161
703-605-6000

This report is available in electronic form at http://www.sti.nasa.gov/ and http://ntrs.nasa.gov/

Heat Transfer Measurements and Computations on Blade of Variable Speed Power Turbine Blade Cascade

Philip E. Poinsatte
National Aeronautics and Space Administration
Glenn Research Center
Cleveland, Ohio 44135

Douglas R. Thurman
U.S. Army Research Laboratory
Glenn Research Center
Cleveland, Ohio 44135

Paul W. Giel
Vantage Partners, LLC
Brook Park, Ohio 44142

Ali A. Ameri
The Ohio State University
Columbus, Ohio 43210

Barbara L. Lucci
National Aeronautics and Space Administration
Glenn Research Center
Cleveland, Ohio 44135

Summary

Heat transfer measurements were obtained on the blade surface of a two-dimensional section of a variable speed power turbine (VSPT) rotor blade in a linear cascade. Infrared thermography was used to determine the blade heat transfer distribution. Changes in the local heat transfer rates with Reynolds number were used to identify the laminar, turbulent, and transitional flow regimes, as well as to determine regions of flow separation. Steady-state data were obtained for six incidence angles ranging from 15.8° to –51.0°, and at five flow conditions for each angle. Reynolds numbers were varied over an order of magnitude, and two exit Mach number conditions were examined in order to accommodate the facility operating envelope. Additionally, Reynolds-averaged Navier-Stokes (RANS) calculations using the GlennHT computational fluid dynamics code were performed for the cruise and takeoff conditions.

Nomenclature

A total area of heater strip
B Exponent in Eqution (2)
C_{P_t} total-pressure coefficient, $C_{P_t} = \left(P_{t,1} - P_t\right) / \left(P_{t,1} - P_{t,2}\right)$
c_x blade axial chord length, in.
H Blade span

i incidence angle
k thermal conductivity of air
M Mach number
Nu Nusselt number
PR pressure ratio, $PR = P_{t,1}/P_2$
P pressure
Q heater strip power
Re Reynolds number, $\mathrm{Re} = \rho U c_x/\mu$
S blade pitch, in.
s surface distance, in.
T temperature
U total mean velocity
x chordwise (axial) coordinate, in.
y pitchwise (tangential) coordinate, in.
z spanwise coordinate, in.
Zw Zweifel coefficient, $Zw = (2S/c_x)\cos^2\beta_2(\tan\beta_1 - \tan\beta_2)$
β relative flow angle, pitch angle, deg, $\beta = \tan^{-1}(U_y/U_x)$
μ dynamic viscosity
ρ density

Subscripts

1 cascade inlet
2 cascade exit
b baseline
i isentropic
s static
t total

Introduction

Future vertical lift vehicles that can have both vertical takeoff and Mach 0.5 cruise capability will require enabling technologies such as variable speed power turbines (VSPTs) or multiple gear ratios (Refs. 1 and 2) in order to maintain high propulsive efficiency. Future aircraft may require up to 50 percent reduction in the main rotor speed during cruise at nearly constant engine-corrected flow rates. Although a conventional method for reducing turbine speed is through gearing, a potential alternative is designing power turbine blades and vanes to accommodate large variations in incidence flow angle. Technologies using incident-tolerant blading can optimize propulsive efficiency by allowing the power turbine to change shaft speed while minimizing weight and fuel consumption. A VSPT must overcome these large incidence flow angle variations at high work factors and low Reynolds numbers over a wide operational speed range in order to be viable.

Several studies have addressed some of the challenges that are relevant to variable speed turbines. Welch (Ref. 2) provided details of the VSPT technology and the followup technology transitions. Johnson, Yamauchi, and Watts (Ref. 3) and Acree, Yeo, and Sinsay (Ref. 4) described the benefits and challenges of vertical lift and Mach 0.5-cruise-capable rotary wing vehicles such as NASA's Large Civil

Tilt-Rotor (LCTR) concept vehicle. The LCTR was the reference vehicle used as the baseline for several aerodynamic studies performed by NASA and the U.S. Army Research Laboratory. Experimental VSPT studies have been reported in References 5 to 8 detailing aerodynamic performance through five-hole probe surveys at various Reynolds numbers, incidence angles, blade loading, and loss buckets. Computational fluid dynamics (CFD) simulations will be used to design and analyze future VSPT blading. The accuracy of these simulations is highly dependent on their ability to predict laminar, turbulent, and transitional flow regimes, particularly as Reynolds numbers decrease at altitude cruise conditions where separation-induced losses can become prevalent. Low-turbulence experimental data within VSPT blade rows can prove to be challenging test cases for CFD codes and lead to model improvements. The experimental determination of the local laminar, turbulent, and transitional flow regimes, and the identification of any separated flow regimes, is critical to the improvement of CFD predictive capability needed to optimize future VSPT blade designs.

The objective of the present study is to advance the understanding of the aerodynamic effects of large incidence angle and Reynolds number variations in order to address key VSPT challenges. Among the challenges is to improve the computational modeling of complicated flows such as those seen in a VSPT blade row with a wide range of incidence angles and flow rates. In a previous study (Ref. 9), sections of the planar endwall in a linear cascade were heated electrically, and endwall heat transfer distributions were determined using infrared (IR) thermography. This report presents the turbine blade surface heat transfer data for the same cascade. Changes in the local heat transfer rates with Reynolds number were then used to identify the laminar, turbulent, and transitional flow regimes as well as to determine regions of flow separation. The heat transfer measurements in this study were not meant to be used to determine cooling requirements; rather, they are to be used to identify regions of flow transition and separation on the blade surface. A range of Reynolds numbers spanning an order of magnitude was investigated at several incidence angles, similar to studies described in References 5 to 7. The current turbine blade heat transfer surface data, along with the previous endwall data, will provide beneficial information for CFD code and turbulence model improvement and help optimize future incident-tolerant blade designs.

Description of Experiment

Heat transfer measurements on an instrumented blade of the two-dimensional (2D) VSPT blade section were conducted in the Transonic Turbine Blade Cascade Facility at the NASA Glenn Research Center, shown in Figure 1. A description of the facility can be found in Reference 5. The cascade comprises nominally 10 blades that represent a scaled 2D midspan section of the VSPT second-stage rotor based on a Rolls-Royce design. Geometry details are described in Reference 9 and summarized in Table I. The facility has the capability to test large-scale models (span of 6 in. (15 cm)) with continuous flow at engine-relevant Mach and Reynolds numbers. In addition, the cascade is attached to a wheel that can be rotated to provide incidence angles from 15.8° to –51.0°, as shown in Figure 2; this allows for a wide range of incidence angles to be studied. Table II lists the angles that were examined in this study. Inlet air is supplied by a 40-psig (276-kPa) combustion air system, which provides clean, dry ambient-temperature air. The air is then passed through a flow conditioner, a contraction section, and then into the main test section with upper and lower flow boards, finally exhausting through an altitude exhaust system maintained at 2 psia (14 kPa). For the current tests, no inlet turbulence grid was installed, which provided low inlet turbulence intensities of 0.8 percent.

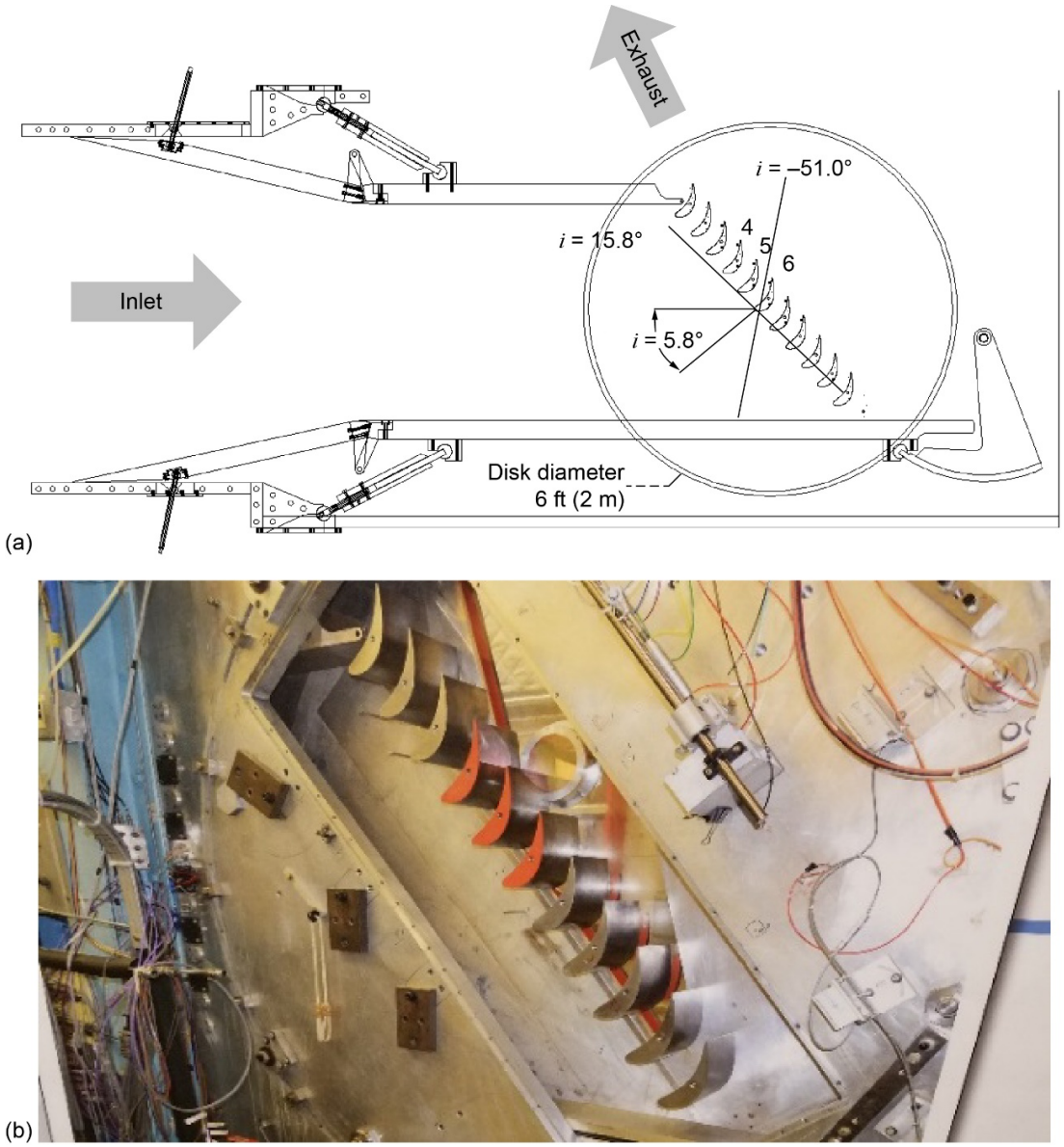

Figure 1.—Transonic Turbine Blade Cascade Test Facility. (a) Cascade wheel. (b) Test section.

TABLE I.—VARIABLE SPEED POWER TURBINE BLADE PARAMETERS

Axial chord length, c_x, in.	7.109
True chord length, in.	7.655
Pitch, S, in.	5.119
Span, H, in.	6.000
Solidity, c_x/S	1.389
Aspect ratio, H/c_x	0.844
Throat dimension, in.	2.868
Stagger angle, deg	20.35
Inlet metal angle, deg	34.2
Uncovered turning, deg	19.47
Exit metal angle, deg	−55.54

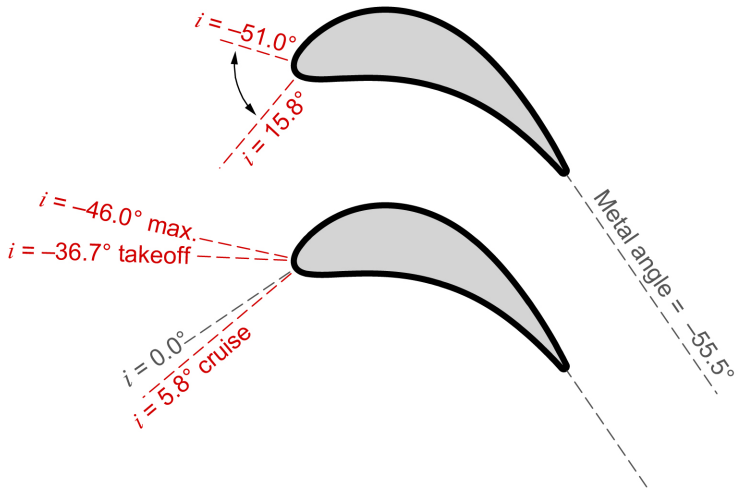

Figure 2.—Incidence angles *i* of variable speed power turbine blade.

TABLE II.—VARIABLE SPEED POWER TURBINE INLET FLOW ANGLES

Incidence angle, *i*, deg	Zweifel coefficient, *Zw*
15.8	1.22
5.8 (cruise)	1.06
–16.1	0.82
–36.7 (takeoff)	0.65
–46.0 (max. mission)	0.58
–51.0	0.53

At each incidence angle setting in Table II, data were acquired at the five nominal flow conditions listed in Table III. The design pressure ratio *PR* of 1.412 was used, which corresponds to an exit isentropic Mach number $M_{i,2}$ of 0.72. A baseline exit Reynolds number, $Re_{c_x,2,b}$, based on axial chord length was determined by finding the lowest Reynolds number at which the tunnel could maintain an $M_{i,2}$ of 0.72, which was found to be 0.53×10^6. Because of limitations of the tunnel operating envelope, the design $M_{i,2}$ could not be reached at the lowest $Re_{c_x,2,b}$ of 0.212×10^6; thus, the $M_{i,2}$ was reduced to 0.35 for these cases. Additional overlap flow points were tested at $M_{i,2}$ of 0.35 and 0.72 at $1.0\times Re_b$. The nominal endwall inlet boundary layer thickness ranged from 1.6 in. (4.1 cm) at the lowest Re to 1.2 in. (3.0 cm) at the highest Re.

The test blade is shown in Figure 3. It was constructed by casting a ~0.25-in. (~0.64-cm) epoxy layer around a foam core. An Inconel sheet with a 0.001-in. (0.003-cm) thickness was wrapped around the blade surface. The Inconel was attached using a double-faced adhesive sheet and tack welded to the bus bar endcaps of the blade.

TABLE III.—VARIABLE SPEED POWER TURBINE
NOMINAL TUNNEL FLOW CONDITIONS

Flow case	Exit Reynolds no., $Re_{c_x,2}$	Reynolds no. baseline factor [a]	Pressure ratio,[b] *PR*	Exit Mach no., $M_{i,2}$
1	0.212×10^6	0.4	1.087	0.35
2	0.530×10^6	1.0	1.087	0.35
3	0.530×10^6	1.0	1.412	0.63 to 0.72
4	1.060×10^6	2.0	1.412	0.72
5	2.120×10^6	4.0	1.412	0.72

[a]Baseline exit Reynolds number, $Re_{c_x,2,b} = 0.530\times10^6$.

[b]Design $PR = 1.412 \rightarrow M_{i,2} = 0.72$.

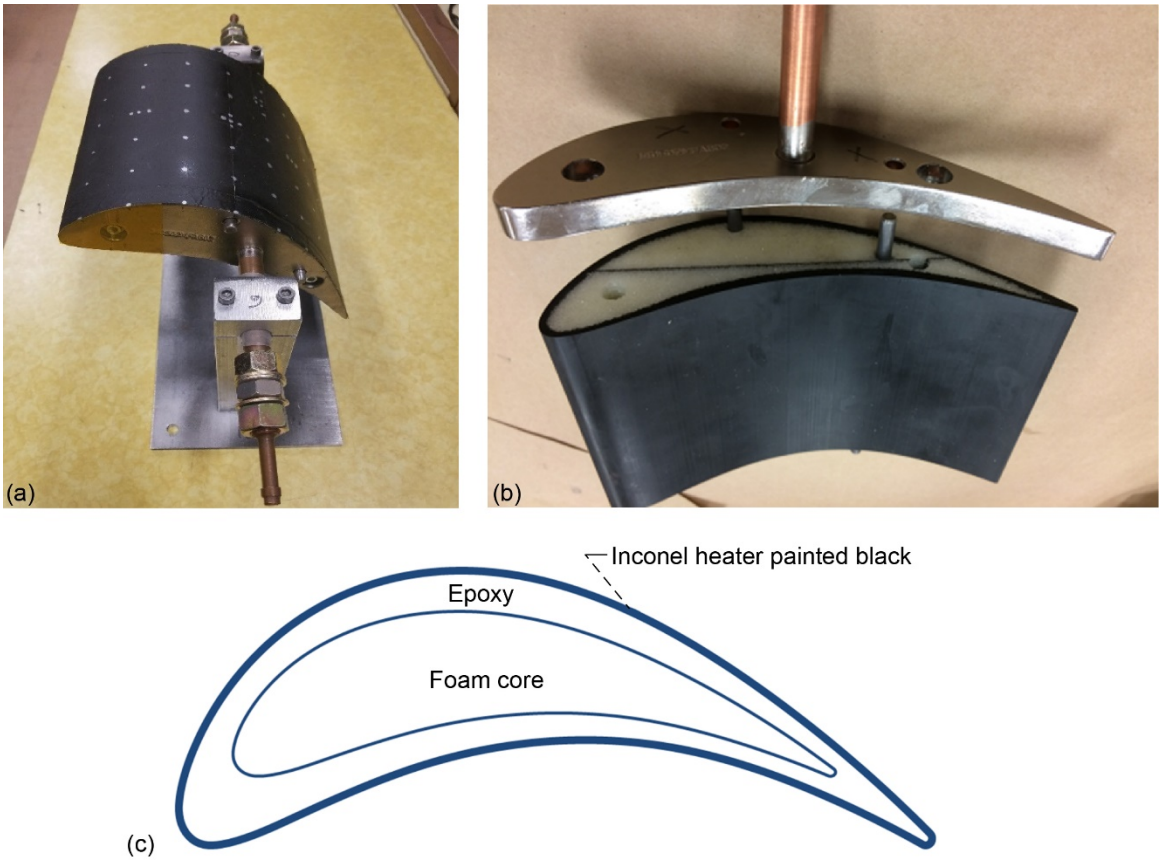

Figure 3.—Variable speed power turbine blade heat transfer test model and cross section. (a) Model. (b) Assembly. (c) Cross section.

Figure 4.—Infrared window ports and cameras in Transonic Turbine Blade Cascade Test Facility.

The heater power was determined through accurate measurements of heater voltage and current. Thin-film thermocouples were each attached to the pressure and suction surface to provide a surface temperature for calibration of the IR thermography images. Each side of the tunnel wall included coated ZnSe IR viewing ports, as shown in Figure 4, which allowed roughly 95 percent transmission of IR radiation. Three FLIR® Systems, Inc., IR cameras were aligned with the viewing ports to image both sides of the blade surface and acquire temperature data on those blade surfaces. One camera was used to view the pressure surface while two cameras were used for the suction side—one upstream and one downstream with an overlap of about 1 in. (3 cm). The IR images of the blade surface were obtained at highly skewed angles, and views were also hindered by cascade blades adjacent to the test blade.

The blade was painted flat black to provide a nominal emissivity of approximately 0.94. A 1- by 1-in. grid of fiducial dots was painted on the surface to assist in correcting the angled and distorted images.

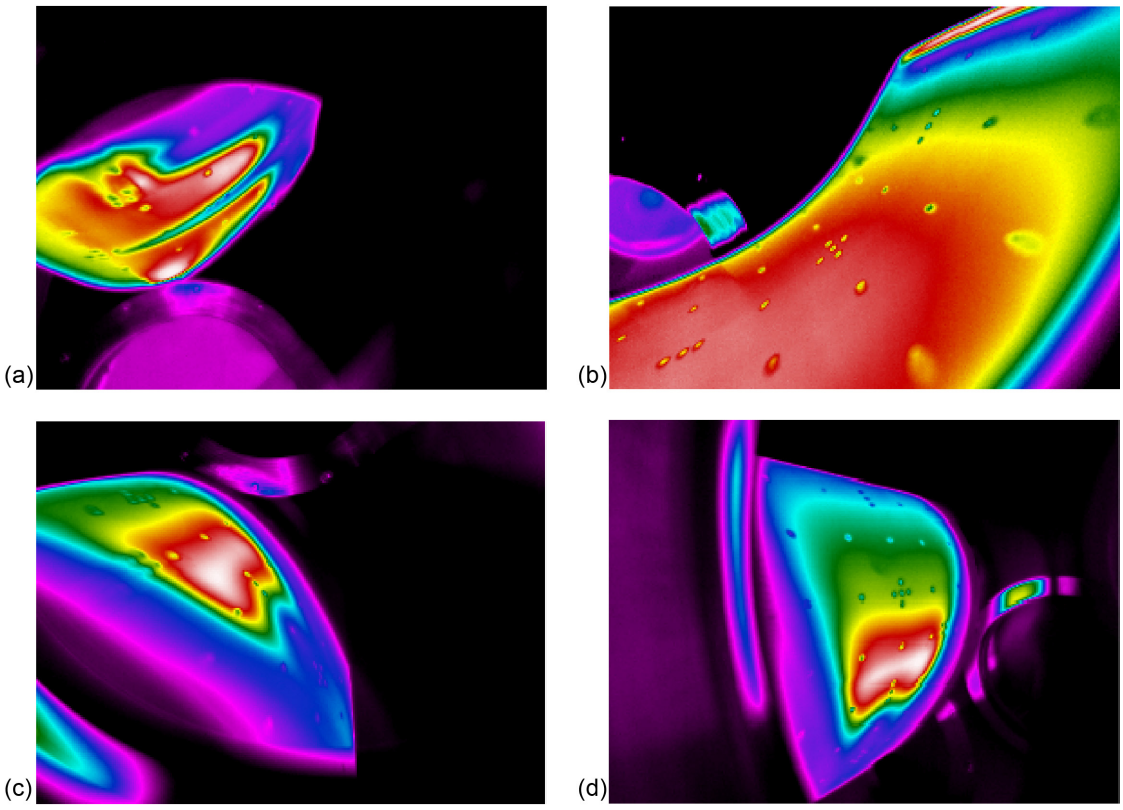

Figure 5.—Typical infrared data images of variable speed power turbine blades. (a) Takeoff suction side. (b) Takeoff pressure side. (c) Cruise suction upstream. (d) Cruise suction downstream.

Nusselt numbers were determined using the following equation:

$$\mathrm{Nu} = \frac{h \cdot c_x}{k} = \frac{Q \cdot c_x}{A \cdot k \cdot \Delta T} \tag{1}$$

in which Q is the heater strip power, A is the total area of the heater strip, c_x is the blade axial chord length, and k is the thermal conductivity of the air. The temperature difference ΔT is the difference between the surface temperatures from an image acquired with heat applied and an image acquired with no heat applied, which approximates the adiabatic surface temperature. The adiabatic surface temperatures were used to account for compressible flow effects. Since the images were taken at highly skewed angles and the cameras were not completely perpendicular to the surface, the Nusselt images were run through a view correction program and converted to unwrapped Cartesian coordinates; the 1-in. (3-cm) grid points were used for this remapping. The emissivity of the various skewed camera views were adjusted to coincide to the thermocouple surface temperatures. The effective emissivities ranged from 0.85 to 0.92. Figure 5 shows examples of typical raw-data IR images acquired. The uncertainty in heat transfer measurements typically ranged between 3 and 10 percent depending on the flow condition, with a few highly curved regions reaching 17 percent. Most of the uncertainty was due to the temperature difference determined from the IR images, which were highly dependent on the estimated emissivity of the test plate.

Figure 6 shows unwrapped blade surface contours of Nu for five flow conditions at the six angles tested. Negative values of surface distance s correspond to the pressure side of the blade, and positive values correspond to the suction side. The dashed lines represent the edges of the full 6-in. span unwrapped airfoil. Note that the contour ranges were scaled such that the flow features were most visible. Thus, while the ranges are consistent for specific flow cases at each angle, the ranges are not the same for all flow cases. For example, the range for flow case 1 is 200 to 1,200 in all figures, but the range for flow case 5 is 1,000 to 5,000. The dots in the data are a result of the silver 1-in. (2.54-cm) grid points on the black painted surface of the blade model. They are manifested in the IR image because of the difference in emissivity of silver dots relative to the black painted surface. In the centerline line plots, occasionally these grid points show up as slight bumps or gaps in the data at regular inch increment locations.

Imaging of the entire curved blade through the viewing ports at various angles was challenging and not always possible. Limitations of the camera viewing ports prevented acquisition of the heat transfer data around the leading-edge region. Also, some of the corners of the contour plots are blocked off; these are regions of the blade model that could not be imaged by the IR camera because of limitations of the viewing angles through the IR window ports. Additionally, some of the data on the pressure side could only be imaged in a 1-in. (2.54-cm) spanwise band across the pressure side length rather than a 2-in. (5-cm) one. For clarity, these data were mirrored into a 2-in. spanwise band. The overlap regions (4 in. $< s <$ 5 in.) of the two suction side camera views were averaged, and in some plots this is visible in the data; for example, Figure 6(b) shows an artifact of the overlapped image averaging from s = 4 to 5 in. Generally, these were well within uncertainty limits. A few figures also show some data anomalies and asymmetry that were typically caused by local trips of the boundary layer that were clearly visible in the raw IR image files. They were caused by small roughness spots on the blade surface. Small dirt accumulations or other protrusions can be large relative to the thin boundary layer on the blade surface and affect the flow. Even the slight height of the applied reference dots were occasional culprits of these local boundary layer trips in some high-velocity situations. (See Figure 6(c) flow case 4 for example; Figure 5(a) shows the raw-data IR image for the same case. Note the low-temperature streak in the midspan of the blade caused by a small protrusion results in a high-heat-transfer streak in Figure 6(c).) These anomalies were left in the data plots, but were generally discounted in the data analysis.

In all cases, as expected, Nu increases with Re. Note that the highest heat transfer on a turbine blade usually is expected at the stagnation region, but again because of viewing limitations of the test rig, data near the leading edge were not able to be measured, especially on the suction side ($s <$ 2 in.). The heat transfer patterns are highly dependent on incident angle. Regions of laminar and turbulent boundary layer flow are evident in the data as are indications of potential flow separation; this will be discussed later.

In a few cases, the effects of secondary flows on the aft section of the airfoil begin to become evident. For example, in Figure 6(f), the tapering regions of high heat transfer on the suction side ($s >$ 6 in.) are a result of the large endwall boundary layer and the impinging of the passage vortex on the suction side of the blade. In general though, this 2-in. span is mostly a 2D flow region, thus a centerline traverse of the data can make the heat transfer analysis easier.

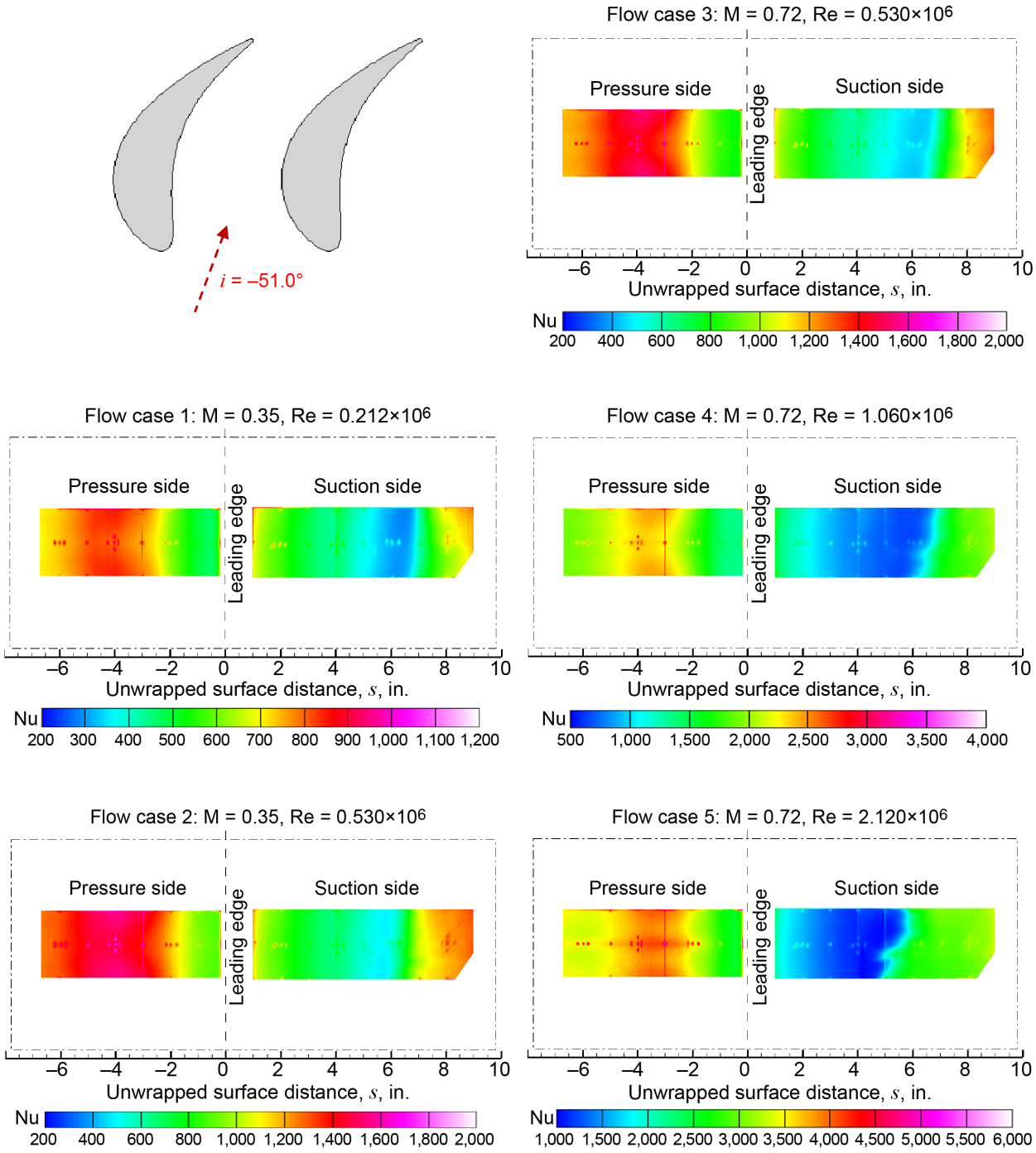

(a)

Figure 6.—Nusselt number (Nu) of VSPT blade surface for five flow cases (different Mach numbers (M) and Reynolds numbers (Re)) at six incidence angles i. (a) i = –51.0°. (b) i = –46.0°. (c) i = –36.7° (takeoff). (d) i = –16.1°. (e) i = 5.8° (cruise). (f) i = 15.8°.

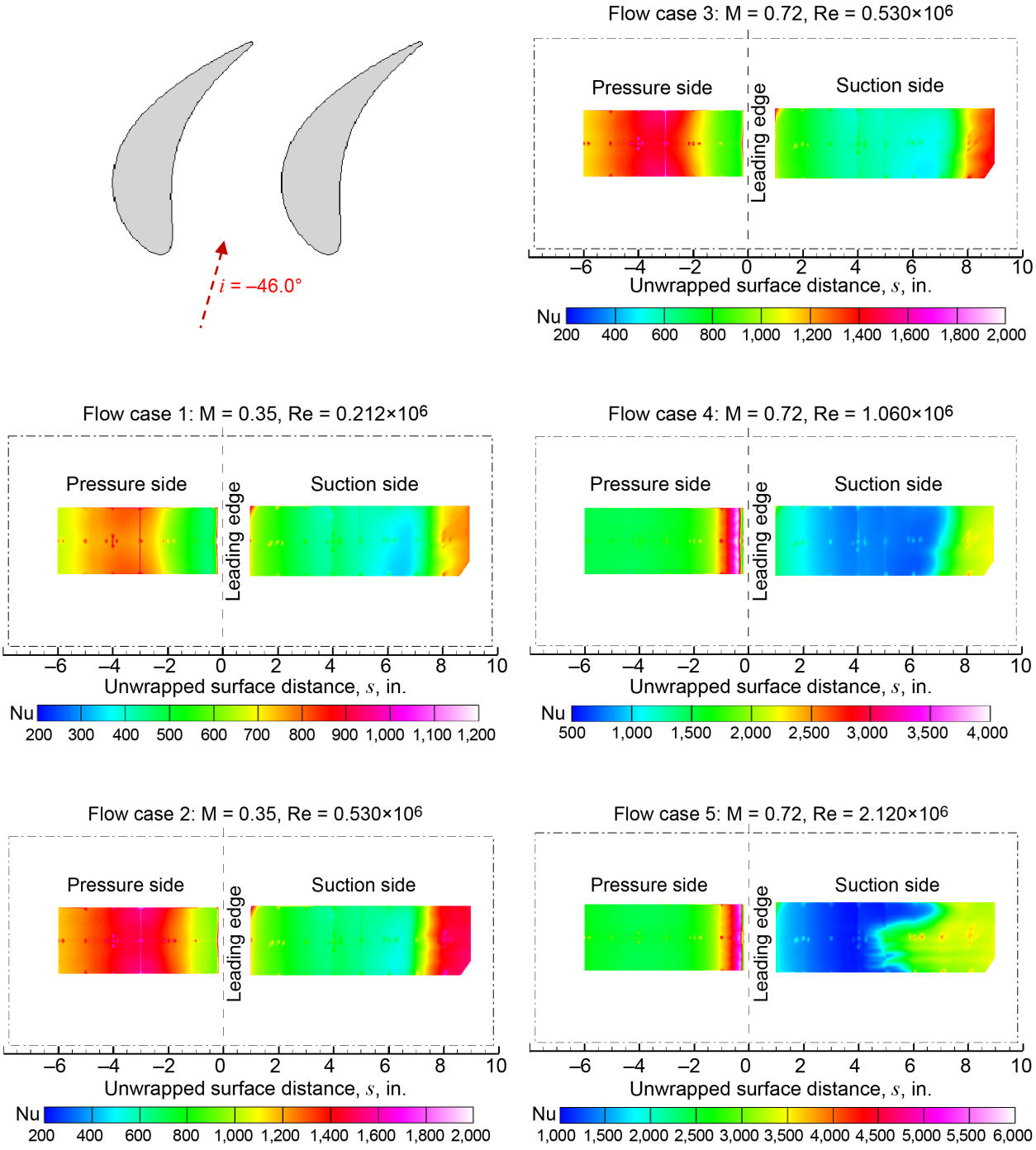

(b)

Figure 6.—Continued.

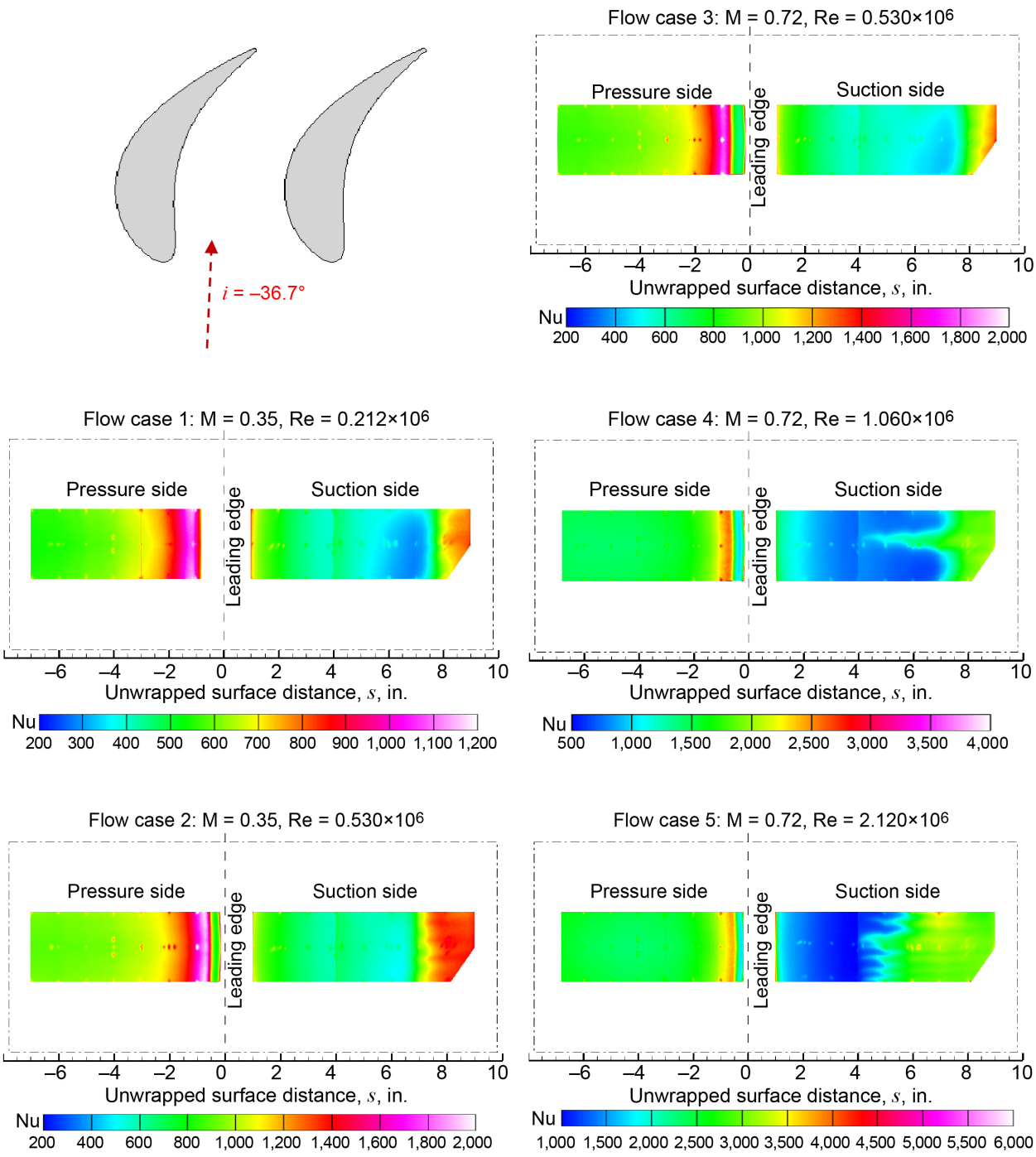

(c)

Figure 6.—Continued.

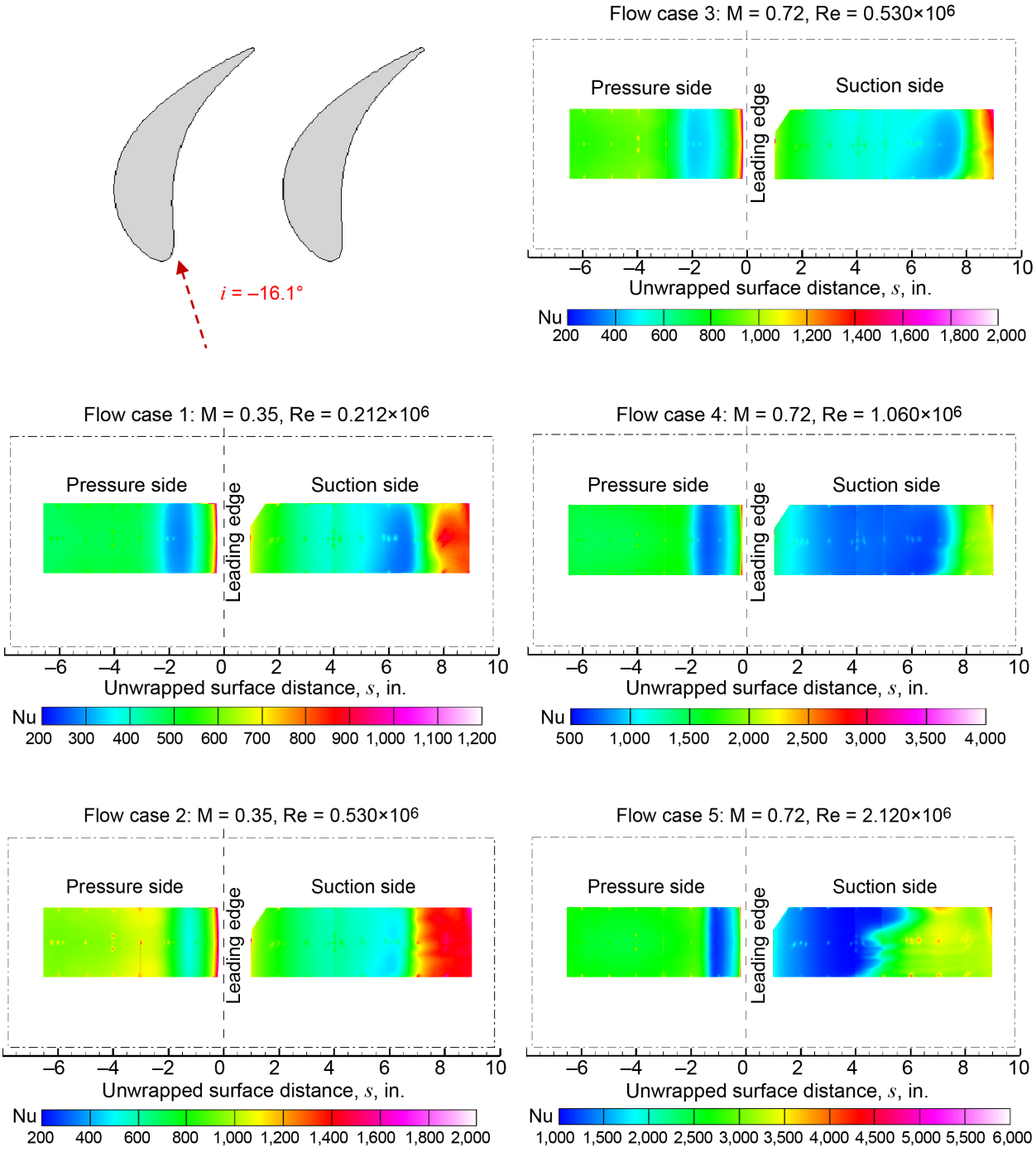

(d)

Figure 6.—Continued.

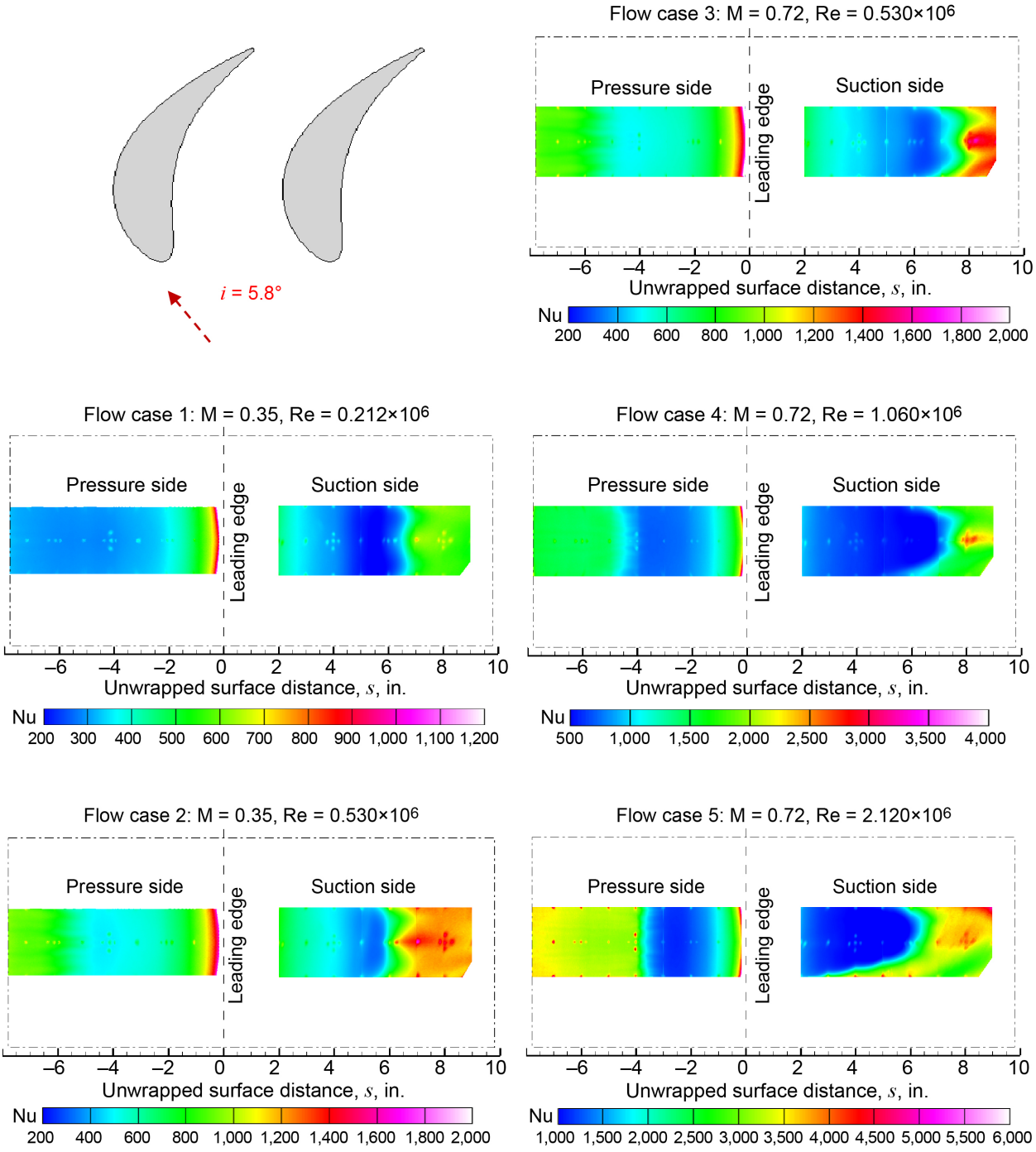

(e)

Figure 6.—Continued.

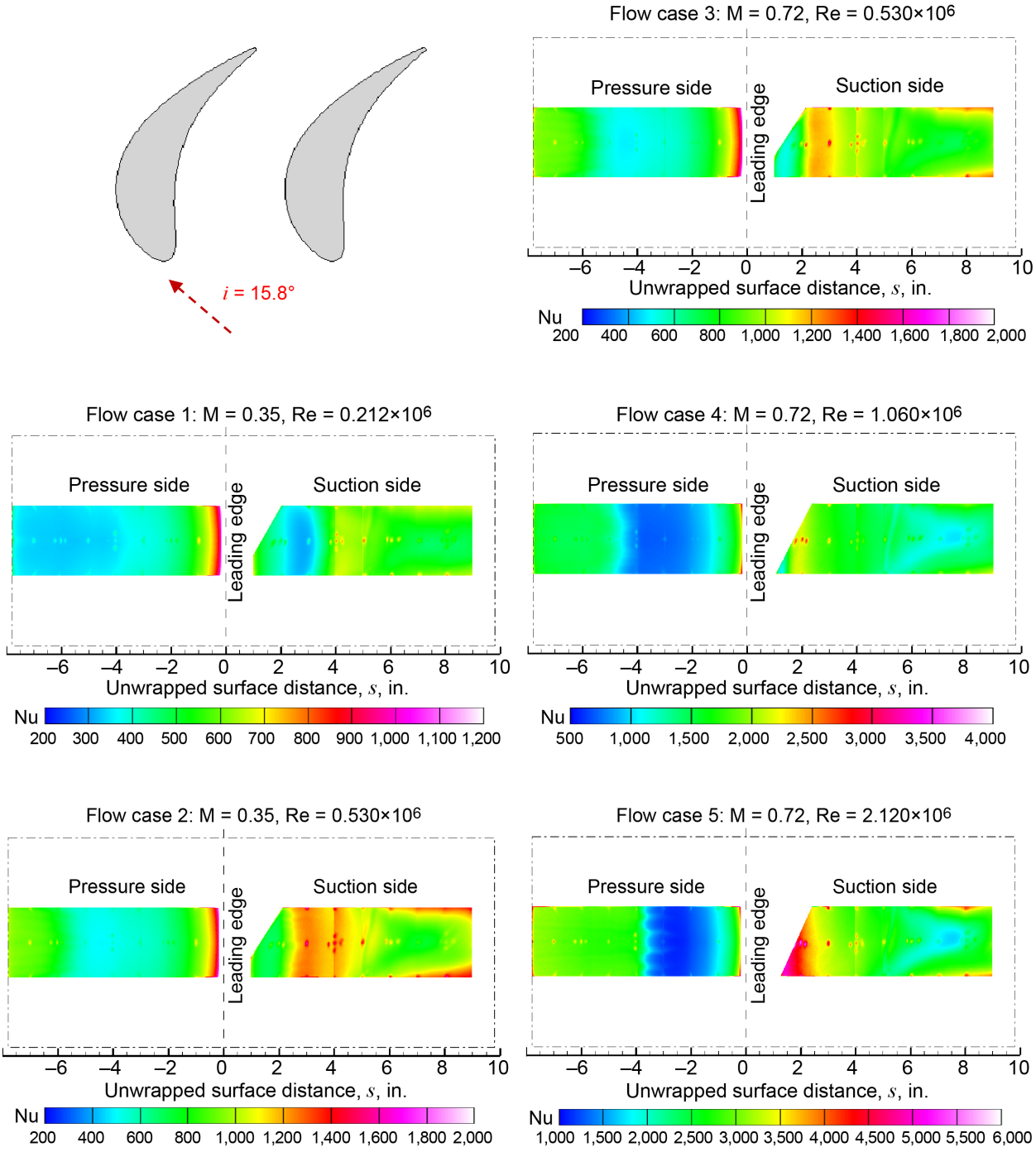

(f)

Figure 6.—Concluded.

Figure 7 shows line plots of span averaged Nusselt number of a 0.25-in. (0.64-cm) band along the centerline of the blade from the pressure side to the suction side for the six angles and five flow conditions tested. Figure 8 shows the blade loading from a previous study of this same blade geometry tested in the same facility (Ref. 5). The centerline plots in Figure 7 clearly show low-to-high heat transfer moving aft along the airfoil, which indicate transition from laminar to turbulent flow; these transition regions will be confirmed with a correlation analysis of the data presented later in this section. Again in all cases, as expected, the heat transfer increases with increasing Reynold number. The flow cases 2 and 3, which nominally have the same Reynolds numbers of 0.53×10^6 but different Mach numbers of 0.35 and 0.72, respectively, generally fall on top of each other—illustrating the relative independence of Mach number on general level of Nusselt number. The only exception is that the higher Mach number alters the blade loading and often moves the transition point downstream. The loading change is evident when comparing flow cases 2 and 3 in Figure 8.

Concentrating first on the cruise condition ($i = 5.8°$), the data in Figure 7(e) indicate laminar flow on the upstream portion of the suction side and turbulent flow on the downstream portion. At a constant M, increasing the Re moves the transition point forward on the airfoil. At M = 0.72, the transition starts at $s = 7.5$ for flow case 3 ($\mathrm{Re} = 0.530\times10^6$), $s = 7$ for case 4 ($\mathrm{Re} = 1.060\times10^6$) and $s = 5.5$ for case 5 ($\mathrm{Re} = 2.120\times10^6$). For M = 0.35, transition starts at $s = 6.2$ for case 1 ($\mathrm{Re} = 0.212\times10^6$) and 5.9 for case 2 ($\mathrm{Re} = 0.530\times10^6$). Note that cases 2 and 3 lines generally fall on top of each other, indicating that the laminar and turbulent heat transfer levels are the same; this is expected since the Re is the same for both cases. The higher Mach number of case 3 though, has delayed the start of transition from s of 5.9 to 7.5. Figure 8 shows that the suction-side loading for case 3 is certainly flatter around x/c_x of 0.7 than for case 2, but the general levels are very similar. Figure 7(e) shows the heat transfer on the pressure side of the blade is high near the leading edge and then quickly drops to a level corresponding to laminar flow. For the lowest flow case, the flow seems to stay laminar all the way to the trailing edge. The cases 2 and 3 data again lie on top of each other throughout and show a slight rise in heat transfer level beginning at $s = -5$. Note the pressure-side loadings of cases 2 and 3 from Figure 8(c) are identical. The higher Re cases 4 and 5 also show an increase in heat transfer at $s = -4$ and $s = -3$ respectively, as the boundary layer transitions to turbulent flow.

The heat transfer patterns for the $i = -16.1°$ flow angle shown in Figure 7(d) are very similar to the $i = 5.8°$ angle, except the transition locations are generally moved close to the leading edge.

Moving to the takeoff condition with an incidence angle of –36.7° (Figure 7(c)), the Nu data show suction-side flow behavior similar to the cruise condition with laminar flow transitioning to turbulent. Increasing Re moves the transition point towards the leading edge. The heat transfer behaviors for cases 2 and 3 are again the same except that the increased M has delayed the transition start from s of ~6.8 to ~7.5. However, the pressure-side Nu data illustrate different flow characteristics than for the cruise case. For all flow cases, the Nu shows a rapid decrease to a local minimum level just past the leading edge and then a rise sharply to a maximum value. The flow then drops and levels off to roughly laminar levels. The slight increase at $s < -4$ at the highest Re may indicate some turbulent flow on the downstream pressure surface; this region will be examined in the correlation analysis later in this section. The dramatic dip near $s = -0.5$ indicates a possible small separation near the leading edge followed by reattachment at $s = -1$. The loading data of Figure 8(c) in the leading-edge region seem to indicate a mostly attached flow with perhaps only a small confined separation bubble; however, the raw temperature for $i = -36.7°$, an example of which is shown in Figure 5(b), certainly shows a hot strip on the pressure side near the leading edge.

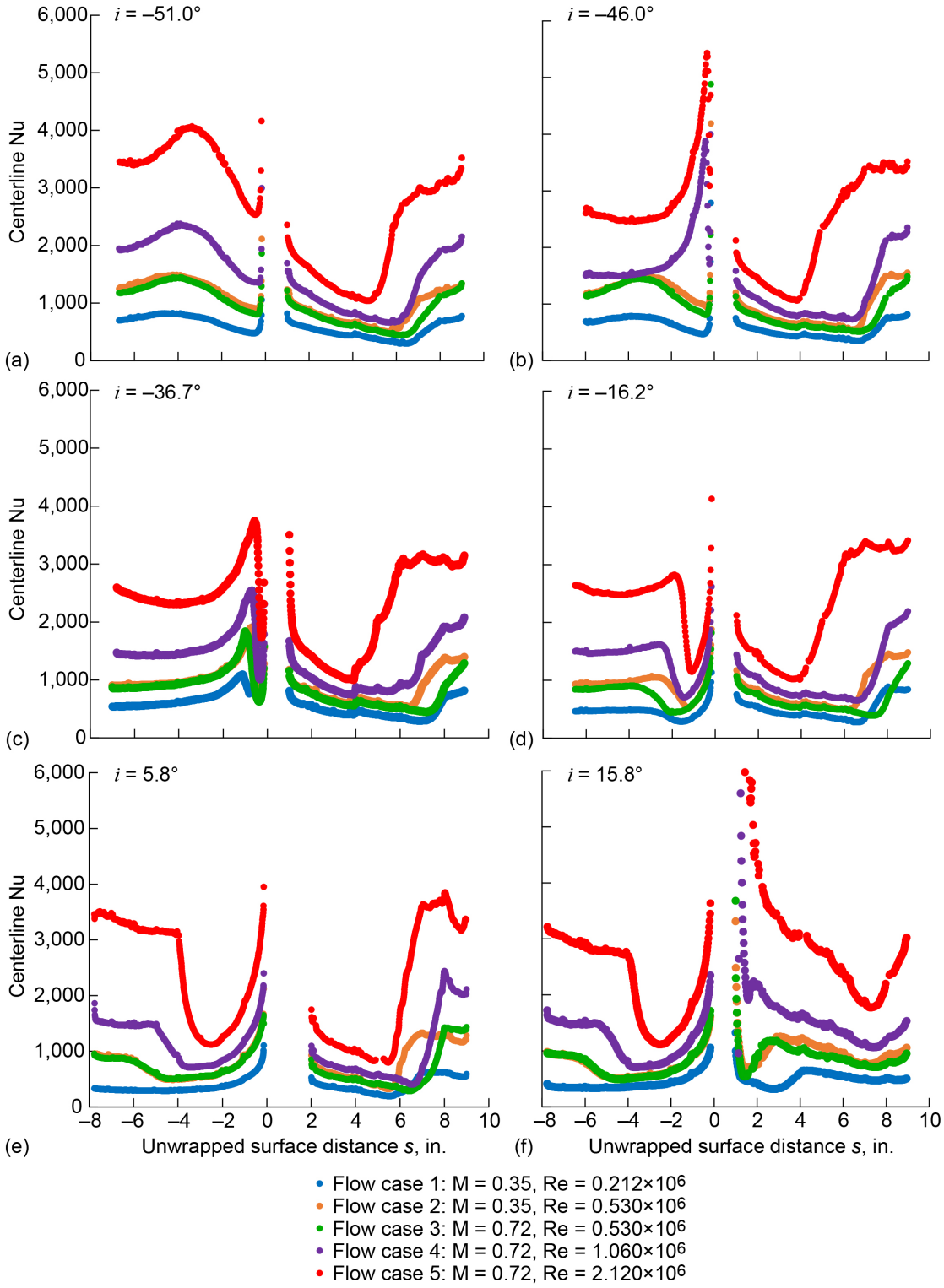

Figure 7.—Centerline average of Nusselt number (Nu) versus unwrapped surface distance from pressure side (negative s) to suction side (positive s) of variable speed power turbine blade for five flow cases (different Mach numbers (M) and Reynolds numbers (Re)) at six incident angles i. (a) i = –51.0°. (b) i = –46.0°. (c) i = –36.7° (takeoff). (d) i = –16.2°. (e) i = 5.8°(cruise). (f) i = 15.8°.

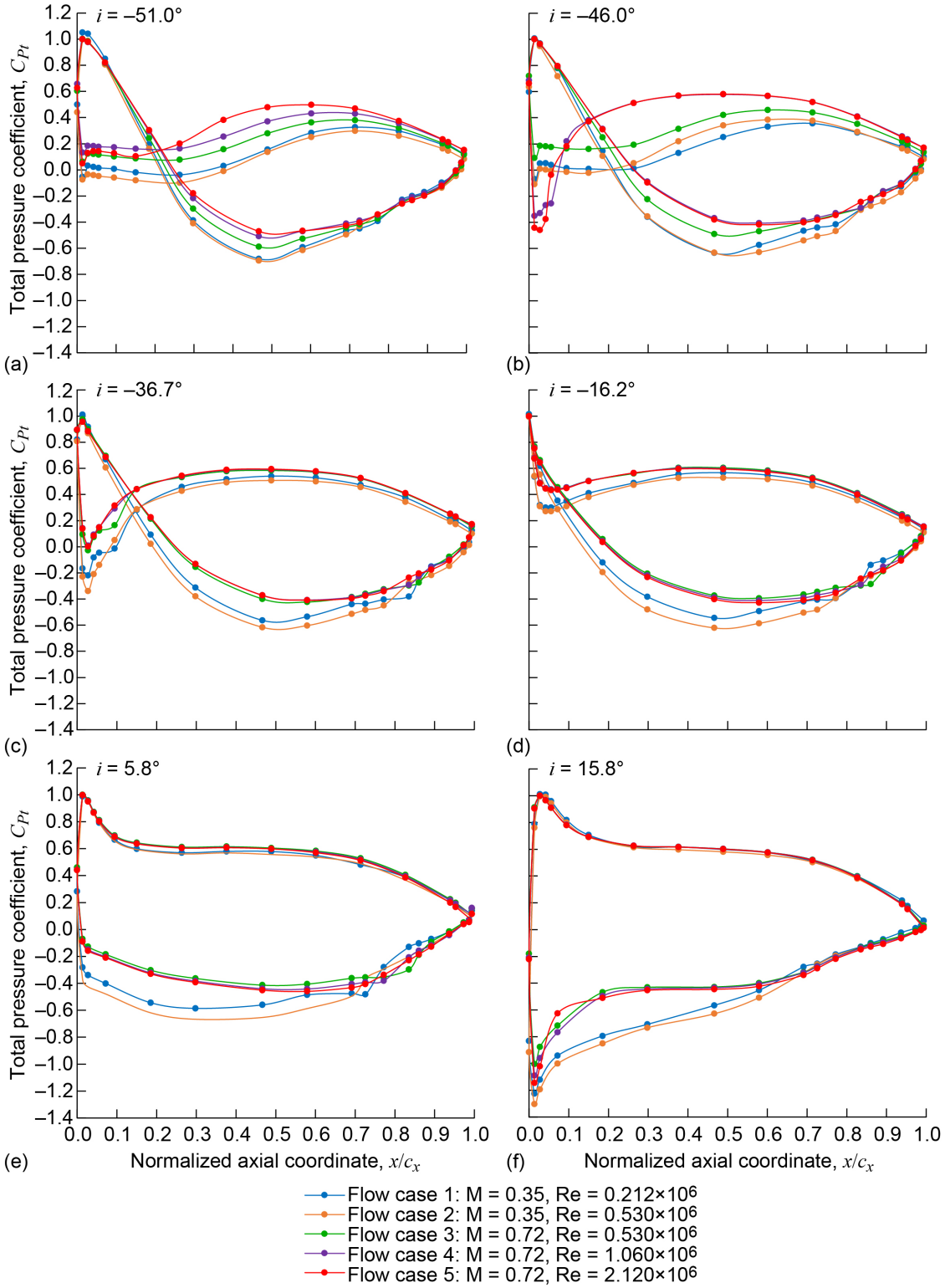

Figure 8.—Variable speed power turbine blade static pressure loading at different incidence flow angles i for five flow cases (different Mach numbers (M) and Reynolds numbers (Re)). c_x is blade axial chord length. Data from Reference 5. (a) i = –51.0°. (b) i = –46.0°. (c) i = –36.7° (takeoff). (d) i = –16.2°. (e) i = 5.8° (cruise). (f) i = 15.8°.

Another interesting feature can be seen by comparing the $i = -51°$, $-46°$, and $-36.7°$ cases. Whereas the suction-side heat transfer patterns are similar, showing laminar flow transitioning to turbulent, the pressure-side heat transfer patterns are not consistent throughout all Re values and angles. The flow may be separating and reattaching on the pressure side, and for some of the lower Re values the flow may be relaminarizing downstream as has previously been reported (Ref. 10). The $-36.7°$ case generally shows a very high heat transfer peak at the reattachment point followed by a decrease to a roughly constant level. The $i = -51°$ case shows a wider peak much further downstream followed by a somewhat decreasing heat transfer level moving downstream. For the $-46°$ angle, the high-Re cases exhibit behavior similar to those at $-36.7°$, but the lower Re cases look similar to those at $-51°$. Additionally, examination of the loading data of Figure 8(a), (b), and (c) show that the pressure-side leading edge flows for the $-46°$ high-Re cases looks like those at $-36.7°$, but those for the $-46°$ low-Re cases looks like those at $-51°$. Thus, the flow patterns and resulting heat transfer are highly dependent on i and not always consistent with changes in Re.

The data for the 15.8° case (Figure 7(f)) show an even more dramatically different heat transfer pattern compared to other angles. On the pressure side, the flow starts as laminar, and for the lowest flow condition, remains so moving aft; however, for the higher flow cases the flow transitions to turbulent moving aft along the blade surface. On the suction side, the heat transfer is very high near the leading edge, especially at the higher Re values. The heat transfer generally decreases moving aft, but remains at a turbulent level. For the lower Re cases, the transition point occurs very early on the airfoil. At this steep incidence flow angle, the flow accelerates very rapidly along the suction-side blade surface.

Figure 9 shows the centerline heat transfer data grouped as a function of Re, showing the effects of angle on heat transfer and transition location at various Re values. It is seen that changing the incidence flow angle dramatically affects the heat transfer pattern. On the suction side, the Nusselt lines are mostly on top of each other and even the location of transition from laminar to turbulent flow is similar. However, at the 15.8° flow case, the heat transfer dramatically increases as the flow seems highly accelerated. On the pressure side, the effect of changing the angle is more pronounced; not only does the transition location change with angle, but regions of separation and relaminaization are also dependent on flow angle.

Flow transition was also investigated by comparing the Nusselt-Reynolds number correlation values for the different flow conditions, where

$$\mathrm{Nu} = A \times \mathrm{Re}^{B} \tag{2}$$

Although this correlation was developed for flow over a flat plate, it is still useful in determining where flow transitions from laminar to turbulent on the turbine blade surface. Plotting local values of the exponent B calculated from multiple flow conditions gives an indication of the state of the local boundary layer as the flow transitions from one condition to another. For a flat plate, a value for B of 0.5 indicates laminar flow, and a value of 0.8 indicates turbulent flow. Guzovic (Ref. 11) determined generalized statistical correlations for various sections of blade surface for flow conditions ranging from laminar through turbulent. The correlation yields values of $A = 0.123$ and $B = 0.6785$ for the overall blade surface. Guzovic also showed that using data in only the trailing-edge region correlated better with values of $A = 0.0021$ and $B = 0.9777$. The current data from all flow cases at each incident angle was fit to this form in which the coefficient A was forced to 0.123, and B was determined locally by a least-squares data fit using all five flow cases. Figure 10 shows the Guzovic correlation for the blade surfaces for all six incidence flow angles. The B values range from 0.6 to 0.75, which are typical values that Guzovic found for the blade surfaces. Generally, the B value is higher at the trailing edge, which also agrees with Guzovic's results.

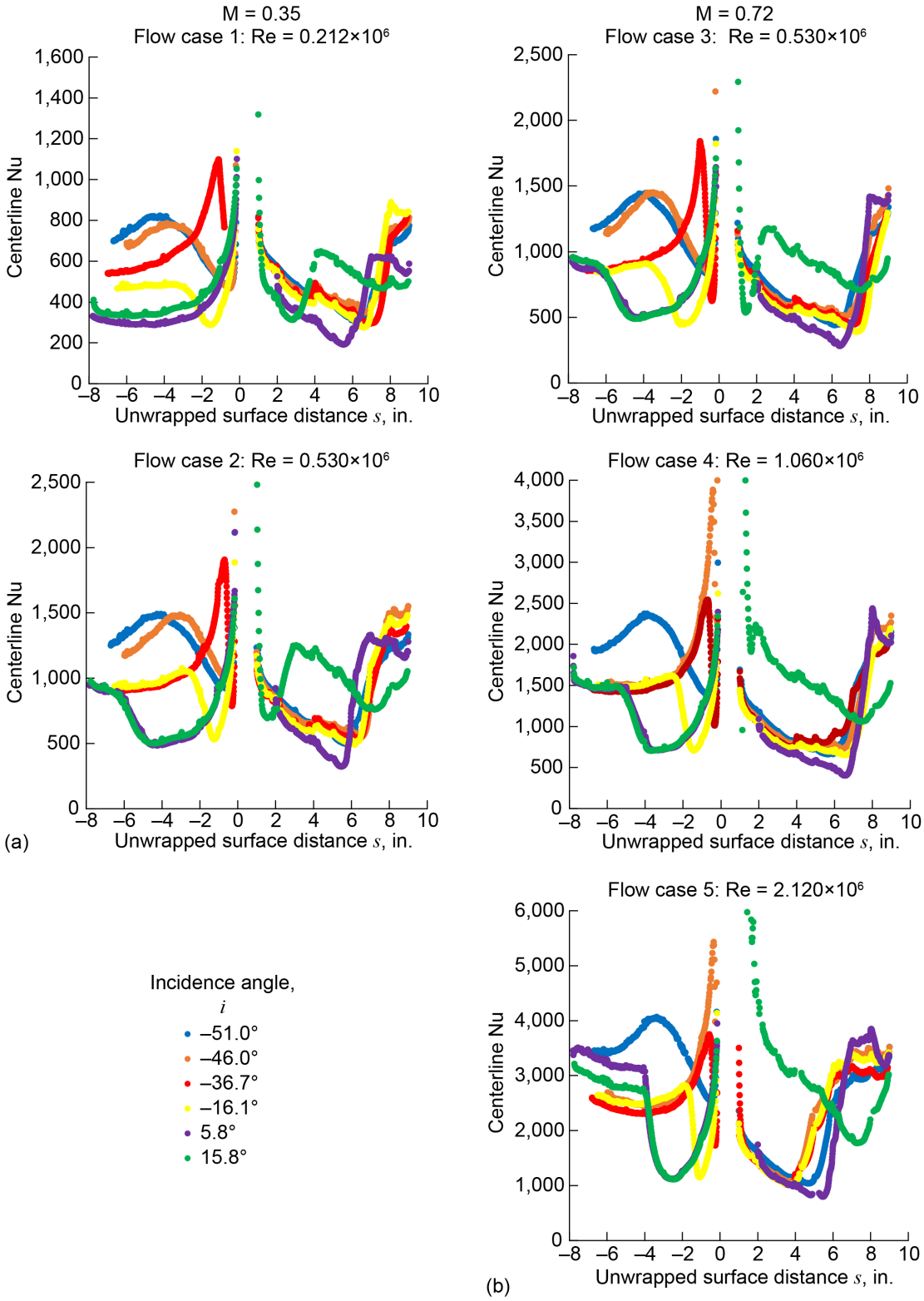

Figure 9.—Centerline average of Nusselt number (Nu) versus unwrapped surface distance from pressure side (negative s) to suction side (positive s) of variable speed power turbine blade for six incidence angles i at five flow cases (different Mach numbers (M) and Reynolds numbers (Re)). (a) M = 0.35; case 1: Re = 0.212×10^6 and case 2: Re = 0.530×10^6. (b) M = 0.72; case 3: Re = 0.530×10^6, case 4: Re = 1.060×10^6, and case 5: Re = 2.120×10^6.

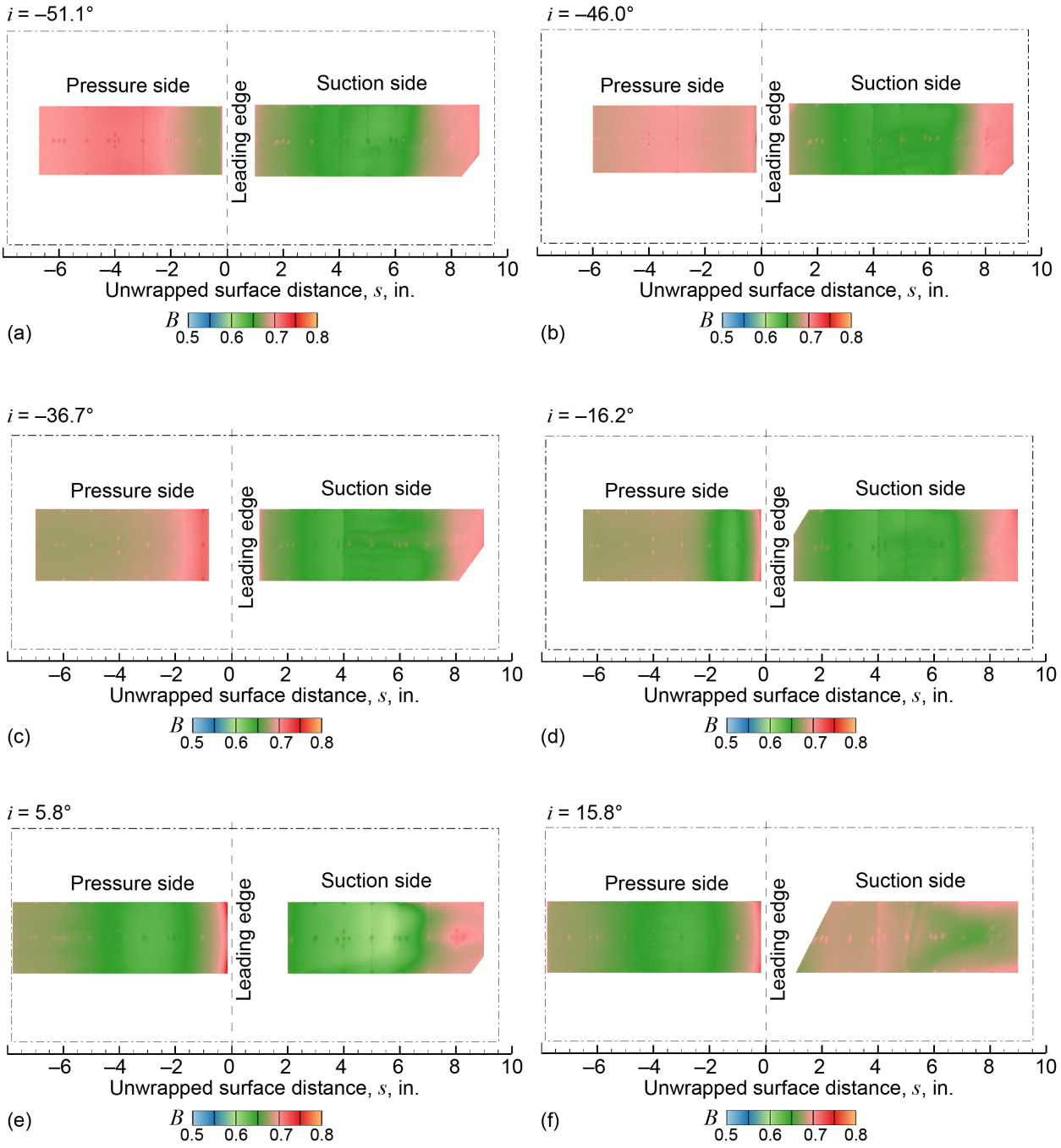

Figure 10.—Values of exponent B from Nu = $A \times \mathrm{Re}^{B}$ using Guzovic correlation values for A (Ref. 11) in present data for all Reynolds number cases at six incidence flow angles i. (a) i = –51.0°. (b) i = –46.0°. (c) i = –36.7° (takeoff). (d) i = –16.2°. (e) i = 5.8° (cruise). (f) i = 15.8°.

Although the analysis of Reference 11 provides an overall average indication of flow status, the local flow can better be evaluated by examining cases of similar Mach number to determine if any regions of laminar flow are evident. A least squares fit of Equation (2) using only flow cases 1 and 2 (M = 0.35, see Table III) and a least squares fit using flow cases 3, 4, and 5 (M = 0.72) yields the B values in Figure 11. As previously stated, values of $B = 0.5$ indicate areas of laminar flow and values of 0.8 indicate areas of turbulent flow. The areas of very high B ($B > 1.0$) are artifacts of comparing Nu dependence from two flow cases where the transition from laminar to turbulent flow region has moved on the blade surface. Thus, the high-B regions clearly show the boundary layer transition zones along the blade surface. Generally, the transition point moves forward with increasing Re. Thus, the very high B region results when a turbulent region is correlated with a laminar region. The upstream edge of the high-B region corresponds to the transition point of the higher flow case, and the downstream edge corresponds to the transition location of the lower flow case.

For angles of –16.1°, 5.8°, and 15.8°, the pressure side indicates laminar flow near the leading edge (blue) followed by a transition region (red) and turbulent flow (green) moving aft. Comparing the lower and higher Mach number cases, similar behavior is seen, except that the transition region has indeed moved forward on the airfoil as previously noted. The suction side generally exhibits similar behavior of laminar flow transitioning to turbulent flow moving aft along the airfoil, although the transition regions seem to be larger and more sensitive to small changes in flow conditions. Again, increasing Mach number generally moves the start of transition forward. On the suction side, both the 5.8° and 15.8° angle cases display slight indications of a triangle pattern in the data downstream; these are the result of endwall boundary layer and passage vortices working their way to the blade midspan on the downstream sections past $s > 5$. The asymmetry was caused by severe image distortion in the raw data that could not be corrected. Additionally, for the 15.8° case, the suction-side flow is turbulent very near the leading edge, but there is some hint of relaminarization downstream. The 5.8° and 15.8° cases also show an anomaly near $s = 5$; it is uncertain whether this is a real flow phenomena or an artifact of possible image glare.

The suction side of incidence angles –36.7°, –46°, and –51° show laminar flow near the leading edge transitioning to turbulent flow moving downstream. The angles –46° and –36.7°, especially in the high-Mach cases, show evidence of pressure-side flow separation near the leading edge followed by reattachment around $s = –0.5$ for –36.7° and $s = –1$ for –46°. The reattachment shows generally high heat transfer and regions of turbulent B values, but interestingly this is followed by lower B values, indicating a relaminarization of the flow. The flow perhaps begins a slow transition to turbulent, moving toward the trailing edge; at least the higher flow cases for –36.7° do show some transition to turbulent flow for $s < –4$. There is some indication of pressure-side relaminarization on the –51° case as well, although much less pronounced.

GlennHT Computations

GlennHT is a second-order finite volume solver that solves the compressible Navier-Stokes equations in conservation form (Ref. 12). The present computations use a RANS scheme that applies a three-equation turbulence and transition model developed by Walters and Cokljat (Ref. 13). The boundary conditions employed matched the experiment conditions, including a constant wall heat flux and use of a no-heat case for adiabatic approximation.

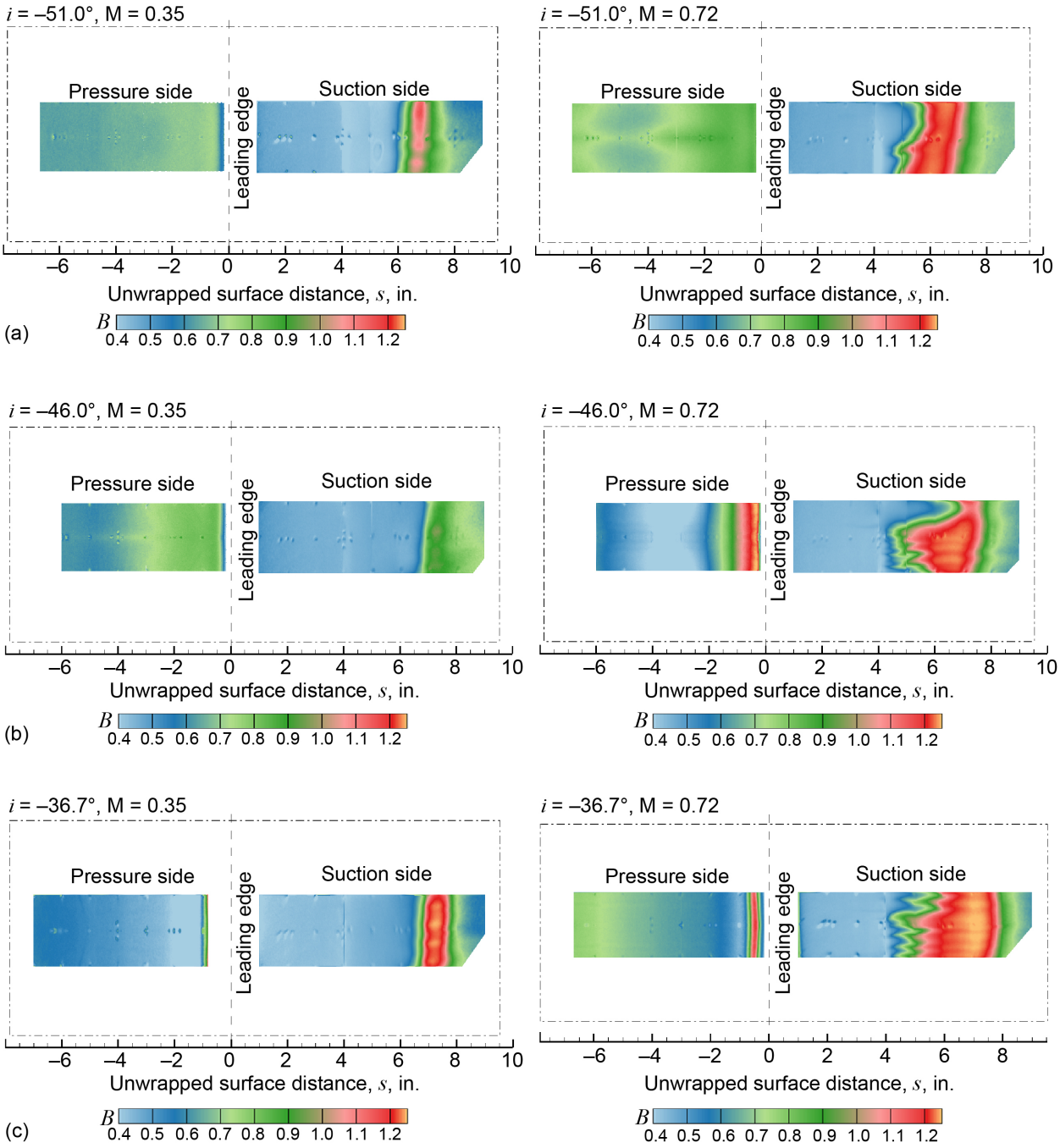

Figure 11.—Values of exponent B from Nusselt number correlation for Mach number M = 0.35 and M = 0.72 flow cases at six incidence flow angles i. (a) i = –51.0°. (b) i = –46.0°. (c) i = –36.7° (takeoff). (d) i = –16.1°. (e) i = 5.8° (cruise). (f) i = 15.8°.

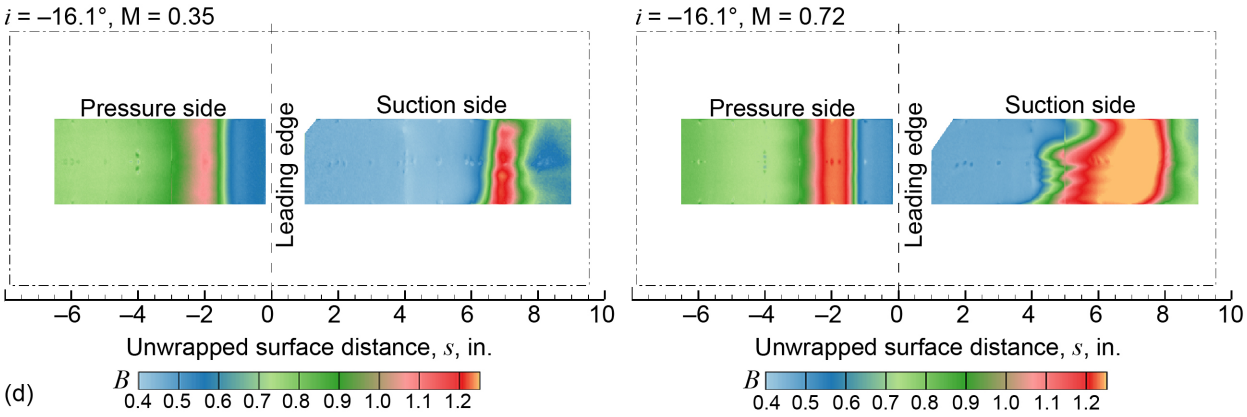

(d)

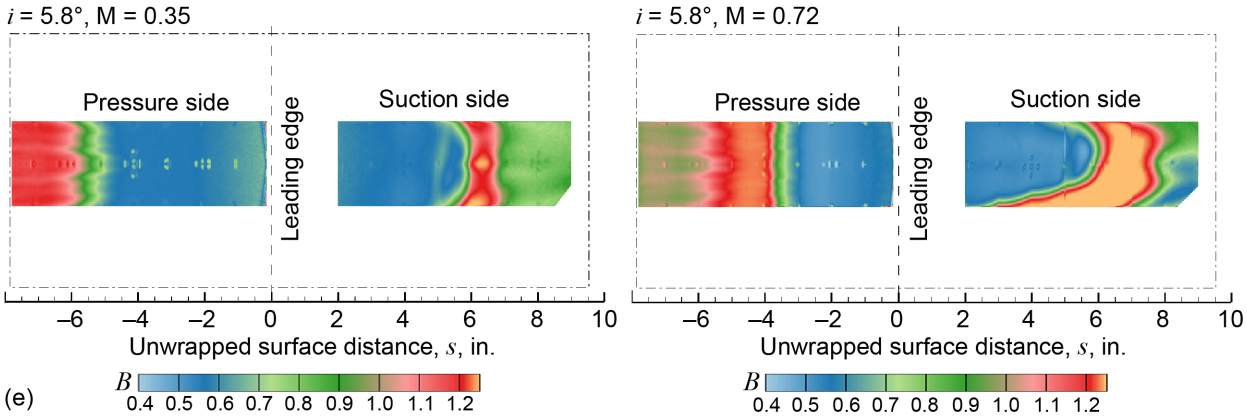

(e)

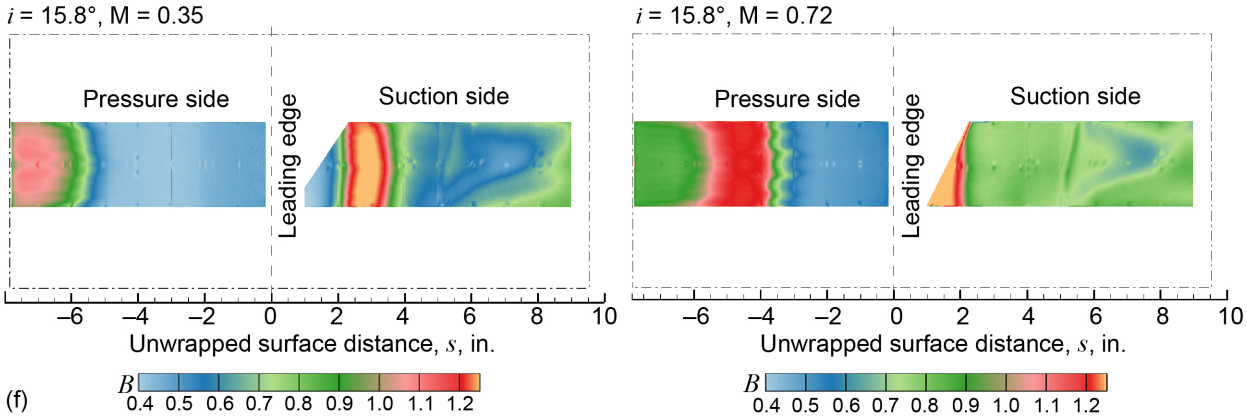

(f)

Figure 11.—Concluded.

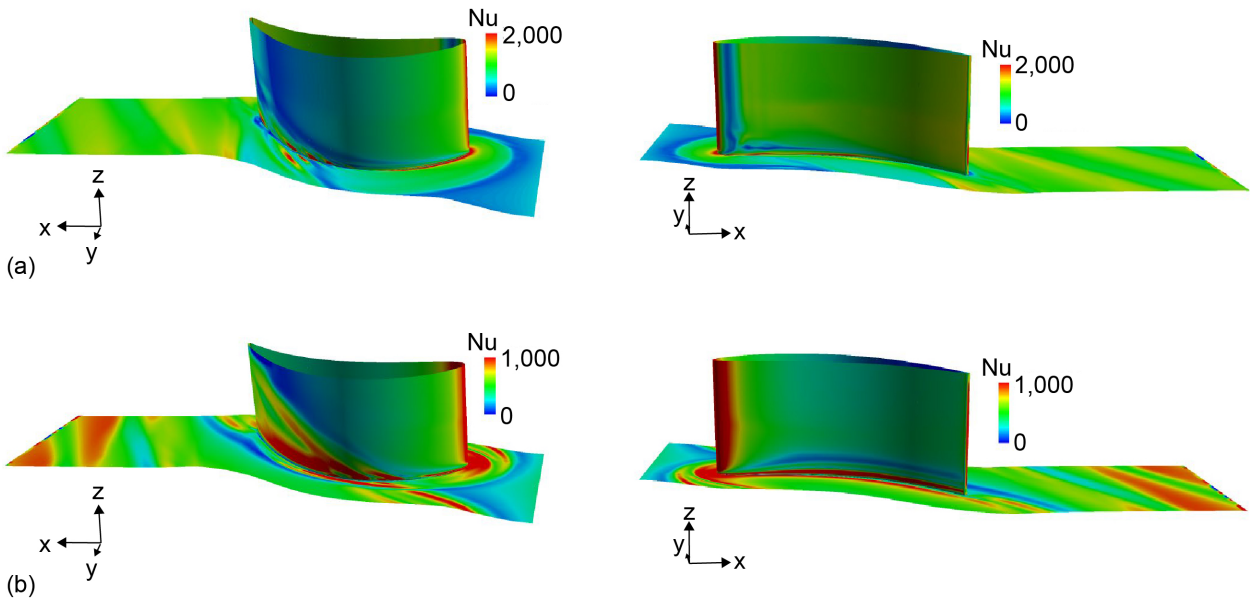

Figure 12.—GlennHT computations of Nusselt number (Nu) on blade suction and pressure surfaces for Reynolds number Re = 0.530×10^{6} at takeoff and cruise. (a) Takeoff: incidence angle i = –36.7°, Mach number M = 0.67. (b) Cruise: i = 5.8°, M = 0.72.

Figure 12 shows plots of Nu from GlennHT of the VSPT blade. The simulations are for the takeoff (–36.7°) and cruise (5.8°) angles at Re = 0.530×10^{-6}. The contour plots are half-span views of the blade and show the complicated heat transfer patterns on the endwall and the suction and pressure sides of the blade. The effects of the horseshoe and passage vortices and other related secondary flows on the endwall and blade are clearly visible.

Figure 13 shows a comparison of the blade symmetry-line traces of the heat transfer of the GlennHT prediction and the centerline experimental data for takeoff (–36.7°) and cruise (5.8°) angles at two Re values (0.530×10^{-6} and 2.120×10^{-6}). Again, the negative values represent the pressure surface of the blade and the positive values represent the suction side. The GlennHT centerline of Figure 13 corresponds to the top of the contour plots of Figure 12. For the lower Reynolds number case, the agreement with data is quite good at both of the incidence angles. For the 5.8° incidence, the suction-side heat transfer data show transition for both the experimental data as well as the simulation. The Nu past the transition point does not rise as high for the simulation; in fact, the simulation shows signs of separation. On the pressure side, the experimental data show transition, but the simulation does not. Also on the pressure side, the flow separates just past the leading edge and immediately reattaches, which produces fully turbulent flow downstream.

For the high-Re cases at 5.8° incidence, the suction-side level of Nu and the location of transition agree with the data, but the Nu levels past the point of transition do not agree. On the pressure side, the experimental data show transition, whereas the simulation does not. For the takeoff case (–36.7°), the pressure-side heat transfer during the separation and reattachment process does not agree well with the data, but the turbulent regime downstream agrees quite well. On the suction side, the simulation shows a transition point that is much farther downstream compared to that of the experiment.

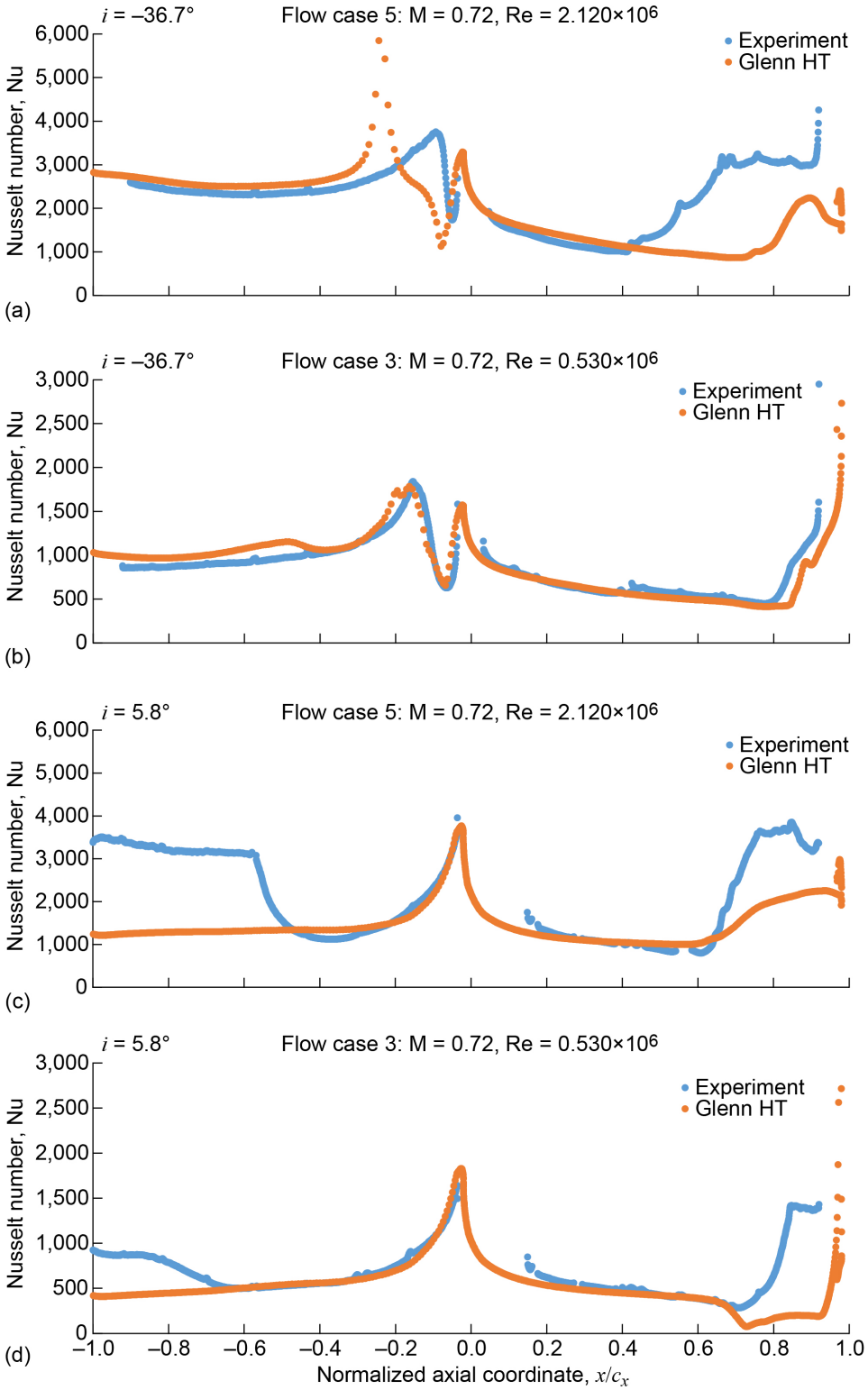

Figure 13.—GlennHT computations of Nusselt number (Nu) on along centerline at flow cases 3 and 5 for takeoff and cruise. c_x is blade axial chord length. (a) Takeoff, incidence flow angle i = –36.7°; Reynolds number (Re) = 2.120×10^6 and Mach number (M) = 0.72. (b) Takeoff, i = –36.7°; Re = 0.530×10^6 and M = 0.67. (c) Cruise, i = 5.8°; Re = 2.120×10^6 and M = 0.72. (d) Cruise, i = 5.8°; Re = 0.530×10^6 and M = 0.72.

Conclusions

The effects of flow transition and separation were investigated experimentally and computationally over large variations in incidence angle and Reynolds number. Infrared thermography was used successfully to determine the state of the boundary layer on a two-dimensional turbine blade of a variable speed power turbine cascade at low turbulence intensity. Heat transfer measurements on the blade surface were acquired for several incidence flow angles and flow rates, showing the complicated dependency of flow angle, Reynolds number, and even Mach number on laminar, turbulent, and separated flow. A Nusselt-Reynolds number correlation provided insight for where transition from laminar to turbulent flow as well as relaminarization may occur along the blade surface. Relative to the experiment, the Reynolds-averaged Navier-Stokes (RANS) computations show general agreement of heat transfer levels, but the location of transition is still not accurately reproduced.

References

1. D′Angelo, Martin: Wide Speed Range Turboshaft Study. NASA CR–198380, 1995. http://ntrs.nasa.gov
2. Welch, Gerand E.: Assessment of Aerodynamic Challenges of a Variable-Speed Power Turbine for Large Civil Tilt-Rotor Application. NASA/TM—2010-216758, 2010. http://ntrs.nasa.gov
3. Johnson, Wayne; Yamauchi, Gloria K.; and Watts, Michael E.: NASA Heavy Lift Rotorcraft Systems Investigation. NASA/TP—2005-213467, 2005. http://ntrs.nasa.gov
4. Acree, C.W., Jr.; Yeo, Hyeonsoo; and Sinsay, Jeffrey D.: Performance Optimization of the NASA Large Civil Tiltrotor. NASA/TM—2008-215359, 2008. http://ntrs.nasa.gov
5. Flegel-McVetta, Ashlie B.; Giel, Paul W.; and Welch, Gerard E.: Aerodynamic Measurements of a Variable-Speed Power-Turbine Blade Section in a Transonic Turbine Cascade at Low Inlet Turbulence. NASA/TM—2013-218069 (GT2013–94695), 2013. http://ntrs.nasa.gov
6. Flegel, Ashlie B.; Giel, Paul W.; and Welch, Gerard E.: Aerodynamic Effects of High Turbulence Intensity on a Variable-Speed Power-Turbine Blade With Large Incidence and Reynolds Number Variations. AIAA 2014–3933 (NASA/TM—2014-218137), 2014. http://ntrs.nasa.gov
7. Flegel, Ashlie B., et al.: Complementary Aerodynamic Performance Datasets for a Variable Speed Power Turbine Blade Section From Two Independent Transonic Turbine Cascades. ISABE2015–20163, 2015.
8. Ford, A., et al.: Design Optimization of Incidence-Tolerant Blading Relevant to Large Civil Tilt-Rotor Power Turbine Applications. NASA/CR—2012-217016, 2012. http://ntrs.nasa.gov
9. Thurman, Douglas, et al.: Heat Transfer Measurements on the Endwall of a Variable Speed Power Turbine Blade Cascade. NASA/TM—2018-220033, 2018. http://ntrs.nasa.gov
10. Giel, Paul W., et al.: Heat Transfer Measurements and Predictions on a Power Generation Gas Turbine Blade. ASME 2000–GT–0209 (NASA/TM—2000-210021), 2000. http://ntrs.nasa.gov
11. Guzovic, Zvonimir; Matijasevic, Branimir; and Rusevljan, Miroslav: Generalized Correlations for Heat Transfer Determination in Turbine Cascades. J. Mech. Eng., vol. 47, no. 8, 2001, pp. 468–475.
12. Steinthorsson, E.; Liou, M.-S.; and Povinelli, L.A.: Development of an Explicit Multiblock/Multigrid Flow Solver for Viscous Flows in Complex Geometries. AIAA–93–2380, 1993.
13. Walters, D. Keith; and Cokljat, Davor: A Three-Equation Eddy-Viscosity Model for Reynolds-Averaged Navier–Stokes Simulations of Transitional Flow. J. Fluids Eng., vol. 130, no. 12, 2008, pp. 121401–121401-14.